Icarus 409 (2024) 115854

Contents lists available at ScienceDirect

Icarus

journal homepage: www.elsevier.com/locate/icarus

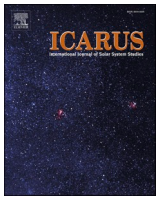

Quantitative analysis of the Martian atmospheric dust cycle: Transported mass, surface dust lifting and sedimentation rates

María Ángeles López-Cayuela [a], María-Paz Zorzano [b,*], Juan Luis Guerrero-Rascado [c,d], Carmen Córdoba-Jabonero [a]

[a] Atmospheric Research and Instrumentation Branch, Instituto Nacional de Técnica Aeroespacial (INTA), Carretera de Ajalvir km. 4, 28850 Torrejón de Ardoz (Madrid), Spain
[b] Centro de Astrobiología (CAB), CSIC-INTA, Torrejón de Ardoz, 28850, Torrejón de Ardoz, Madrid, Spain
[c] Andalusian Institute for Earth System Research (IISTA-CEAMA), 18006 Granada, Spain
[d] University of Granada (UGR), 18071 Granada, Spain

ARTICLE INFO

Keywords:
Data reduction techniques
Atmospheres
Dynamics
Dust
Mars

ABSTRACT

The atmospheric dust cycle on Mars plays a dominant role in the planetary radiative balance, atmospheric photochemistry escape, and redistribution of materials on the surface. Although this planetary dust cycle has been extensively modelled and characterized with both orbital and in situ observations, to date little is known about the total mass of dust that is circulated, the actual dust lifting and settling rates, and the main dust sources and sinks. Using orbital global and seasonal measurements of atmospheric dust opacity, a data reduction methodology that can describe the annual dust redistribution cycle on a planetary scale with 95% accuracy is presented. The method was applied to the 9.3 μm infrared observations of the Thermal Emission Spectrometer (TES) aboard the Mars Global Surveyor (MGS) during two full Martian Years (MY) 25 and 26, and partly MY 24 and MY 27, disregarding the global dust storm that occurred in MY 25. By comparison with terrestrial observations, a mass-to-extinction conversion factor of 1.9 ± 0.3 g m^{-2} is proposed, assuming a dust density of 2.6 g cm^{-3}. The analysis shows an estimation of 400 10^{12} g of dust transported globally in the atmosphere for a typical Mars year, which is comparable to the minimum total annual mass of dust transported on Earth. The methodology proposed here is based on remote sensing and cannot disentangle completely local surface lifting and sedimentation rates from dust advection. However, this analysis provides upper bounds which can be compared with in-situ observations. The analysis of the dust sedimentation cycle suggests that the annual cycle might produce a dust layer of about 50–100 μm on the surface of some particular zones, as Valle Marineris or Meridiani Planum. This estimation agrees with in-situ observations of rovers on Mars. The potential dust sources are mainly located from latitudes of 20°S to 60°S. Our results find the 70% of the sources previously identified by the existing planetary circulation models. This kind of large-scale analysis can be applied to other remote sensing observations to refine these calculations and study the annual and geographical variability of the dust-mass transport on Mars.

1. Introduction

The atmospheres of the terrestrial planets Earth and Mars share a similar origin, but their evolution has diverged significantly (Hart, 1978) due to differences in their masses, distances from the Sun or orbital parameters. On Mars, the convergence of reduced surface gravity and the absence of a significant internally generated magnetic field approximately 700 million years after the planet's formation implied a substantial loss of the atmosphere into interplanetary space (Chassefiére and Leblanc, 2004). The Martian atmosphere is thinner and exhibits a distinct composition compared to Earth's. Specifically, the Martian atmosphere primarily comprises CO_2, H_2O, N_2 (together with its products), and noble gases (Krasnopolsky, 2011), and dust and ice crystals are the only aerosols present. In contrast, Earth's atmosphere is mainly composed of N_2, O_2, Ar and trace gases, and contains a wide variety of both natural and anthropogenic aerosols.

Despite these dissimilarities, both planets have a key common atmospheric feature: the dust cycle, which plays a crucial role in their

* Corresponding author.
E-mail address: zorzanomm@cab.inta-csic.es (M.-P. Zorzano).

https://doi.org/10.1016/j.icarus.2023.115854
Received 23 May 2023; Received in revised form 11 October 2023; Accepted 31 October 2023
Available online 4 November 2023

respective climate systems thanks to its influence on the energy balance (Albani and Mahowald, 2019; Kahre et al., 2017, and references therein). On Mars, dust also has a strong screening effect on the incidence of UV radiation on the surface (Atreya et al., 2006; Córdoba-Jabonero et al., 2003, 2005; Holmes et al., 2021; Zorzano and Córdoba-Jabonero, 2007), thereby influencing the atmospheric photochemistry and habitability. Moreover, dust can play a role in planet-wide mass distribution, particularly in the dispersal and shielding of bioburdens from landed Martian spacecraft (Olsson-Francis et al., 2023).

Particularly on Mars, dust has a repetitive cycle on a large scale, with a certain level of inter-annual variability (Fenton et al., 2007; Read and Lewis, 2004; Leovy, 2001; Wang et al., 2021). Thus, extensive research has been conducted on dust properties to facilitate enhancements in Martian climate models. One important dust property is the opacity (τ), a measure of light extinction as a combination of absorption and scattering processes, produced solely by the aerosol component of the atmosphere. Some relevant works study the columnar-integrated τ (e.g., Montabone et al., 2015, 2020) whether other works are focus on the τ vertical distribution (e.g., Heavens et al., 2011; Kleinböhl et al., 2009).

Most observations of Martian atmospheric dust have been made by spacecraft, which have provided large and validated databases of seasonal and regional atmospheric changes. A comprehensive overview of Martian dust observations from the orbit can be found in Fenton et al. (2016). Among all the available datasets, it is noteworthy to mention the extensively validated and publicly accessible dust database obtained from the Thermal Emission Spectrometer (TES) aboard the Mars Global Surveyor (MGS). This database has been widely utilized to provide global coverage of radiance observations at infrared wavelengths (Christensen et al., 2001). One of the products that provides TES is columnar-integrated opacity (τ), a measure of light extinction as a combination of absorption and scattering processes, produced solely by the aerosol component of the atmosphere. In this work, the columnar-integrated opacity has been used. Using this optical property and applying a dust mass-to-extinction conversion factor (ξ), it is possible to estimate the total mass of dust involved in the dust cycle. To the best of the author's knowledge, explicit results regarding the total quantity of dust mass mobilized during a typical Martian climatic year have not been provided yet.

Several authors have made great efforts to propose this ξ from orbital measurements (e.g., Heavens et al., 2011; Forget and Montabone, 2017). However, little is known about the specific shape, density, and composition of dust aerosols. To date, there have been no analyses of airborne mineral particles and only a few measurements have been taken from the surface. The future Mars Sample Return Campaign is expected to fill this gap in knowledge, bringing atmospheric Martian dust to the Earth for further analysis. But until then, this fact is an issue to be considered, as having precise knowledge of the aforementioned dust properties is crucial in determining a reliable ξ. Thus, this study proposes a complementary quantitative analysis method using Martian orbital dust opacity observations together with some earth-based estimates of ξ.

On Earth, there is extensive knowledge about the airborne dust properties given the enhanced coverage in both spatial and temporal domains, and the extensive dataset of surface, balloon-based and remote sensing observations. Measuring such properties on Mars is considerably more challenging. However, characterizing terrestrial atmospheric dust particles is no straightforward task. On Earth, there is considerable variability of dust mixtures and sources, and their properties can vary regionally or globally. Moreover, there are different products formed by interaction with other aerosols and atmospheric components (DeMott et al., 2003; Karydis et al., 2013), as well as changes that occur during aerosol transport (Stevens, 2015). The scientific community studying terrestrial aerosols has made significant efforts in the detection and quantification of dust suspended in the Earth's atmosphere. To accomplish this challenge, the use of instruments onboard satellite platforms, ground-based remote sensing instrumentation and operational algorithms was employed. Examples of the former include the European Meteosat (Jankowiak and Tanré, 1992) and American NOAA AVHRR (Husar et al., 1997; Swap et al., 1992). As for the latter, it is noteworthy to mention the establishment of the NASA Aerosol Robotic Network (AERONET) (Holben et al., 1998; https://aeronet.gsfc.nasa.gov/) in the 90's. AERONET is composed of a large number of ground-based photometers deployed worldwide. This network uses two types of photometric measurements (direct-sun irradiances and the angular distribution of diffuse sky radiation) and improved aerosol retrieval algorithms (Dubovik and King, 2000; Sinyuk et al., 2020) to provide aerosol columnar optical and microphysical properties across a wide range of regions, such as the τ or the size distribution. The collection of these data demonstrated that these properties differ from one region to another (Schuster et al., 2012) depending on their mineralogical composition. Recent studies (Ansmann et al., 2019; Mamouri and Ansmann, 2017) utilized these AERONET data from major terrestrial deserts to determine a representative ξ for each of these dust sources, that can be used to estimate dust mass loading.

Another important aspect of studying the dust cycle on both planets is the identification of sources and sinks, as well as the characterization of transport. As mentioned before, the existence of a large series of spatial-temporal observations on Earth facilitates this study to a certain extent, but the availability of these measurements is limited on Mars. Thus, it is complicated to quantify the relative distributions of Martian dust over the planet and dust lifting sources based only on observations. However, some lifting processes have been observed directly or inferred from the sudden growth of dust loading in a given region (Fenton et al., 2016, and references therein). These dust observations have been used to feed models, such as the Mars General Circulation Model (MGCM), to model and validate the dust-lifting mechanisms responsible for the Martian dust cycle (Kahre et al., 2006; Newman et al., 2002a; Newman et al., 2002b; Newman and Richardson, 2015; Shirley et al., 2019). It is well known that the dust on Mars is transported through the atmosphere by regional and/or global dust storms (Battalio and Wang, 2021; Haberle, 1986). The Martian surface is covered by aeolian dust, which forms consolidated deposits over time (Mangold et al., 2009). Dust-covered regions have low thermal inertia and can be easily mapped when they are visible from the orbiters. In particular, the thermal inertia cartography obtained by the Viking Infrared Thermal Mapper (IRTM) and the MGS/TES (Christensen, 1986; Jakosky et al., 2000) demonstrated the existence of widespread dust deposits in areas such as the Tharsis Montes, Amazonis Planitia, Elysium Mons, and Arabia Terra on Mars. These dust-laden regions may function as either sources or sinks for Martian dust.

To date, there has been no study on orbital data to quantify the effective dust lifting rates, transported dust mass, and surface thickness of dust layers that may be produced by dust settling. The methodology proposed here is based on remote sensing and we expect that there may be difficulties to disentangle completely local surface lifting and sedimentation rates from dust advection. However, this analysis should be able to provide upper bounds to these rates, to quantify the mass of dust involved in this process and to be compared with the few in-situ observations that exist to date. Finally, this study presents a methodology that allows the quantification of some features of dust transport and settling on Mars, and compares the results with those observed on Earth.

2. Methodology

2.1. TES data and atmospheric dust extinction

In this study, the robust and well-validated dust climatology from MGS/TES was selected. This dust climatology has been widely used by the Martian research community (e.g., Guzewich et al., 2013; Montabone et al., 2015; Sheel and Haider, 2016; Smith et al., 2000) and covers the period of two whole Martian Years (MY) 25 and 26, and partly MY 24 and MY 27. Particularly for this analysis the τ retrievals from the nadir 9.3 μm infrared spectra database (τ^{IR}; Smith, 2004) were selected,

which only τ data flagged as "good quality" in the NASA Planetary Data System (PDS) release were used.

High-quality control criteria were applied in the PDS database to eliminate unreliable values, but this resulted in a lack of data that affected not only the polar regions (mainly in winter owing to the low temperature of the surface) but also the high latitudes in winter (when the surface-atmosphere thermal contrast was too small). Further information on the high-quality control criteria applied to the PDS database can be found in Smith (2004) and Montabone et al. (2015).

In addition, two assumptions were made for TES dust opacity retrieval. First, dust was assumed to be well-mixed with CO_2 gas in the atmosphere; hence, τ could be scaled to 610 Pa to remove the effect of topographic inhomogeneity (Smith, 2004). Second, the retrieval assumes the absence of aerosol scattering. Dust scatters, but a fortuitous combination of the three effects results in almost completely cancelling scattering effects over much of the TES spectral range (Wolff and Clancy, 2003). These factors are the low-to-moderate single scattering albedo values (negligible multiple scattering, $\sim$ 0.1–0.4 near its peak absorption, i.e., 825 cm^{-1} for water ice and 1075 cm^{-1} for dust), the extended nature of the emitting surface during nadir viewing and the broad diffraction peak of the phase functions.

Thus, these assumptions imply that TES provides an effective absorption τ instead of a full extinction τ, with the difference between them being close to a factor of 1.3 (Smith, 2004; Wolff and Clancy, 2003; Wolff et al., 2006). In addition, a conversion IR-to-visible factor of 2.0 was applied (Clancy et al., 2003; Forget and Montabone, 2017; Lemmon et al., 2004; Lemmon et al., 2015). In this study, the TES-provided absorption τ^{IR} was converted to visible extinction (τ^{VIS}) by applying a constant multiplying factor of 2.6, as proposed by Montabone et al. (2015).

2.2. Mass-to-extinction conversion factors

The columnar dust mass concentration (i.e., mass loading, M_L, g m^{-2}) can be obtained from the dust τ^{VIS} data using a specific mass-to-extinction conversion factor ξ (g m^{-2}), as follows:

$$M_L = \xi\, \tau^{VIS}, \tag{1}$$

Actually, those ξ values can vary depending on the dust particles properties. Thus, it can be calculated as the multiplication of density of dust ρ_{dust} (g m^{-2})and a volume-to-extinction conversion factor c_v (μm), which depends on the specific size distribution and extinction properties

$$\xi = c_v\, \rho_{dust} \tag{2}$$

Regarding Martian dust, several authors have proposed formulas for ξ, e.g. the following expression for c_v can be inferred from Forget and Montabone (2017):

$$c_v = \frac{4\, r_{eff}}{3\, Q_{ext}}, \tag{3}$$

where Q_{ext} is the single scattering extinction efficiency with a value close to 2.5 in the VIS band (Forget and Montabone, 2017; Wolff et al., 2006). In addition, r_{eff} is the effective radius of the dust size distribution and their importance relies on how the Martian climate can be affected by the variation of dust particle size (Wang et al., 2021). The r_{eff} parameter is not constant in time and space and has been reported to vary during dust storms (e.g., Chen-Chen et al., 2021; Clancy et al., 2010). Indeed, the value of r_{eff} considered varies depending on the season and the degree of severity of the storms being studied. It should be mentioned that r_{eff} = 1.4–1.6 μm is generally representative of lower dust loading conditions or background dust scenarios (Wolff et al., 2009). Conversely, considering a r_{eff} = 2 μm allows for better agreement between model results for representing global Mars storms (Bertrand et al., 2020). Indeed, Forget and Montabone (2017) considered a typical value of r_{eff} = 1.5–2.0 μm in the lower troposphere for their analysis, and Wolff et al. (2009) used a r_{eff} ranging from 1.2 to 1.8 μm in their models. Clancy et al. (2003), using TES data, found that most of the retrieved dust visible-to-IR opacity was indicative of r_{eff} = 1.5 μm, decreasing frequently in the northern hemisphere to 1.0 μm but increasing in the southern hemisphere during the MY25 global dust storm to 1.8–2.5 μm. More recent studies found similar results for a typical Martian year (without any global storm), a global mean effective particle size of approximately 1.5 μm was found (Haberle et al., 2019). Thus, by using Eqn 3, the Martian c_v could range from 0.53 μm (for the minimum r_{eff} reported in the literature), through 0.80 μm (for a typical Martian year) and reaching 1.07 μm (during a global dust storm; see Table 1).

Finally, ρ_{dust} refers to the particle density of dust. The particle density of Martian airborne dust has not been directly measured to date. All density estimates are qualitative and based on extrapolations from rocks or regolith densities tabulated on the Earth. Thus, some models assumed a dust density value of 2.5–2.7 g cm^{-3} (e.g., Forget and Montabone, 2017; Bertrand et al., 2020; Wang et al., 2021), which is consistent with terrestrial values (2.6 g cm^{-3}, Hess et al., 1998). The estimates for Martian dust density can be improved and updated in the future once the airborne dust component of the Martian sample return mission is fully characterized in terms of mass density, particle shape, and size distribution. Considering all this information, ξ^{Mars} could range from 1.3 to 2.7 g m^{-2} (see Table 1).

As ξ^{Mars} varies substantially depending on the chosen value of r_{eff}, this study examines terrestrial conversion factors and compares them with those obtained for Mars. On Earth, a large amount of information on dust has been gathered through numerous dust observations, finding that the primary properties of dust vary depending on the source region. These regions are primarily desert and arid areas of the planet. As mentioned before, the optical and microphysical properties of dust are strongly influenced by the mineralogical composition, size, and shape of particles that vary between sources. For instance, the major clay-sized particle minerals for dust aerosols are illite in North Africa and kaolinite in the Sahel, whereas the dust composition in the Middle East is usually dominated by montmorillonite, calcite, and gypsum (Schuster et al., 2012). Regarding Asian dust, phyllosilicates are the most common mineral group in dust particles, mainly illite, smectite, and illite-smectite mixed-layer clay minerals (Jeong et al., 2014). To determine an appropriate terrestrial ξ (ξ^{Earth}) for dust particles from a given source, long-term observations are required. Thus, Ansmann et al. (2019) used the reliable climatology of AERONET products (Level 2.0, Version 3, cloud-screening and quality assurance; Giles et al., 2019) to establish robust values of c_v (necessary to obtain the ξ^{Earth}) regarding different sources. Particularly, they used data from 20 stations located in different dust-influenced regions, close to the deserts of North Africa (Sahara and Sahel), the Middle East, Asia (Gobi and Taklimakan) and America-

Table 1
Volume-to-extinction (c_v) and mass-to-extinction (ξ) conversion factors, at visible wavelengths, for dust on Mars and Earth used in this work and its corresponding references. On Earth, the terrestrial averaged ξ values as obtained for the main dust deserts is shown.

		c_v (μm)	ξ (g m^{-2})	
Mars		0.53–1.07	1.3–2.7	From **Eq. [2] and [3]**
Earth	North Africa	0.68 ± 0.08	1.7 ± 0.2	Ansmann et al. (2019)
	Middle East	0.71 ± 0.08	1.8 ± 0.2	
	Asia	0.78 ± 0.10	2.0 ± 0.3	
	America, Australia	0.89 ± 0.13	2.2 ± 0.3	
Earth-like (averaged)		0.73 ± 0.10	1.9 ± 0.3	

Australia (Great Basin and Great Victoria Desert). Details of how to obtain c_v values are given in Mamouri and Ansmann (2014, 2017) but briefly explained, and applied to the climatology of Ansmann et al. (2019), firstly they used the τ at eight wavelengths (mainly in the VIS range), and the Angström exponent at the 440–870 nm spectral range to select dusty conditions among all aerosol scenarios. They used the particle volume size distribution resolved in 22 logarithmic size classes from 50 nm to 15 μm together with the corresponding data sets of volume concentrations (v_c) and τ Hence, the terrestrial c_v can be computed as follows (Ansmann et al., 2019):

$$c_v = \frac{v_c}{\tau} \tag{4}$$

For representation purposes, Table 1 shows the computed c_v and ξ^{Earth} for the regional-continental mean values: North-Africa, the Middle East, Asia, and America-Australia.

In order to obtain a single value of c_v, an average for the 20 sites selected by Ansmann et al. (2019) was applied, giving a $\overline{c_v}$ value of 0.73 ± 0.10 μm. Note that this $\overline{c_v}$ is within the range of Martian ones. This study suggests to use this $\overline{c_v}$ to obtain an 'Earth-like' uniform ξ, ($\xi^{Earth-like}$) as a representative ξ value for dust on Mars. In addition, ρ_{dust} = 2.6 g cm^{-3} is assumed in this work as a representative value of the Martain ρ_{dust} assumed in the models cited above (e.g., Forget and Montabone, 2017; Bertrand et al., 2020; Wang et al., 2021), and also consistent with terrestrial values (Hess et al., 1998).

Thus, an $\xi^{Earth-like}$ of 1.9 ± 0.3 g m^{-2} was used. This value is within the ξ^{Mars} interval, and close to the possible value for a typical Martian year (2.0 g m^{-2}).

2.3. Calculation of the dust mass suspended in the atmosphere and their equivalent dust thickness

In order to calculate the mass loading, the TES-converted τ^{VIS} was averaged in bins of 2° latitude x 5° longitude. In addition, an average over each 1° solar longitude (L_s) has been performed.

As described in **Section 2.2**, by applying $\xi^{Earth-like}$ (see Table 1) to that TES-derived τ^{VIS} climatology, the mass loading of dust particles suspended in the atmosphere can be estimated along the planet (see **Eq. 1**). Finally, to calculate the amount of mass suspended in the atmosphere, an area weighted-sum has been computed for each degree of latitude and longitude, taking into account that a Martian degree of latitude corresponds to 59.2 km in the equator (Birney et al., 2006).

Finally, the Equivalent total Dust Thickness (EDT, μm) has been computed, i.e., the height of the dust layer if all M_L were precipitated over the surface. Note that the particle porosity was ignored, and all grains were assumed to accumulate compactly. The particle density is assumed to be 2.6 g cm^{-3} (see **Sect. 2.2**) and no dynamic transport has been considered. Thus, our method provides a bound estimation.

A climatology was calculated by averaging the TES MY24–27 data, to generate a typical annual dust cycle on Mars. The global dust storm (GDS) data from MY25 was excluded from the climatology, in order to avoid significant bias in the results.

Without loss of generality, our study is mainly focused on the dusty season, which corresponds to the period of L_s from 150° to 360° (e.g., Forget and Montabone, 2017). It should be considered that the dataset was acquired from orbit within a latitude band of 120° wide, regions between 80°N to 40°S were scanned at the beginning of the season, whereas those from 40°N to 80°S at the end.

2.4. Dust lifting and depletion rates

Having accurate dust lifting and depletion rates estimates of Martian dust is important for tunning atmospheric circulation models. This work proposes a way to calculate the dust lifting and settling rates at large scales by subtracting two consecutive snapshots of dust atmospheric loads and dividing them by the duration of the time period. Thus, the dust lifting and depletion rates of the M_L, (δM_L; g m^{-2} L_s − 1) were calculated as the time sequence differences M_L between two consecutive time slots. It should be noted that the resulting rates will necessarily represent mean values as they rely on large-scale averages and the addition of multiple years of climatology. Positive δM_L values indicate an increase in the M_L of dust particles suspended in the atmosphere at a certain point, whereas negative δM_L values indicate a decrease. Unfortunately, this methodology cannot distinguish what percentage of the increase/decrease is related to dust lifting/depletion and what percentage is related to dust advection. This is a first order approach that can be used to calculate upper bounds of the dust lifting or depletion rate. Future local refinements can be done using in-situ observations from landed spacecrafts.

Regarding the local distribution of dust sources on Mars, the lack of data for some zones in several L_s prevents a clear determination of Martian potential dust sources and sinks. For these cases, M_L was averaged each 5° L_s before calculating δM_L in order to reduce gaps in the maps. For a given region, a positive δM_L value indicates a local increase in the total column of dust mass. This increase can be also attributed to either the inflow of dust from nearby atmospheric parcels or local dust lifting from the surface. Conversely, a negative δM_L value represents a local decrease in the total column of dust mass, which can result from either an outflow of dust towards nearby atmospheric parcels or local dust settling.

To complement the interpretation of the map, regions with positive δM_L were compared to the dust sources as obtained from simulations of Newman and Richardson (2015). The work of Newman and Richardson (2015) investigates the impact of finite surface dust availability on the dust cycle in the MarsWRF General Circulation Model and performs a long finite dust simulation (FINDUST), which lasts 374 years. This simulation consists of 17 stages and, in this work, our results are compared to Stage O (80 years) since this simulation can describe the quasi-steady-state behaviour of Mars (Newman and Richardson, 2015).

3. Results and discussion

3.1. Estimation of the total atmospheric mass loading

Fig. 1a shows the total mass loading of dust particles (M_L) suspended in the atmosphere seen by TES climatology at each L_s. Recent studies have pointed out that a daily average can mitigate effects from a potential strong diurnal cycle of dust crossing sols (Kleinböhl et al., 2020; Wu et al., 2020b). Although this analysis can be alternatively done on a sol-basis, we prefer to focus our climatology on a L_s reference, as we are adding and averaging multiple years and describing seasonal effects.

In Fig. 1, only the dusty season (L_s: 150–360°) is shown, where M_L is integrated for the entire planet and north (NH) and south (SH) hemispheres. M_L also denotes the integrated total mass per unit area hereafter for simplicity. Additionally, Fig. 1b shows the M_L dust lifting and depletion rate (g m^{-2} L_s − 1) in terms of δM_L differences for the dusty season. Note that two periods are highlighted, denoted by episode 1 (ep1; L_s = 210°-245°) and episode 2 (ep2; L_s = 310°-350°). In those episodes, and intense dust activity can be observed, with δM_L values greater than ±150 g m^{-2} L_s − 1 together with high M_L values, which reached maximum values of 100 10^{12} g. Both ep1 and ep2 depict an increase/decrease in atmospheric dust particles. This signal is not solely attributed to seasonal dusty storms; rather, a certain percentage may represent the transport of dust from one region to another, which cannot be discerned through this methodology (see **Sect. 2.4**). Regarding the literature, the seasonal storms occur with a remarkable interannual variability. Some percentage of ep1 and ep2 is caused by the type A and C seasonal storms, which started in the SH between L_s = 205°-240° and L_s = 305°-320° for different Martian years (Kass et al., 2016; Smith et al., 2000).

Regarding M_L, in both hemispheres, minimum values are found in

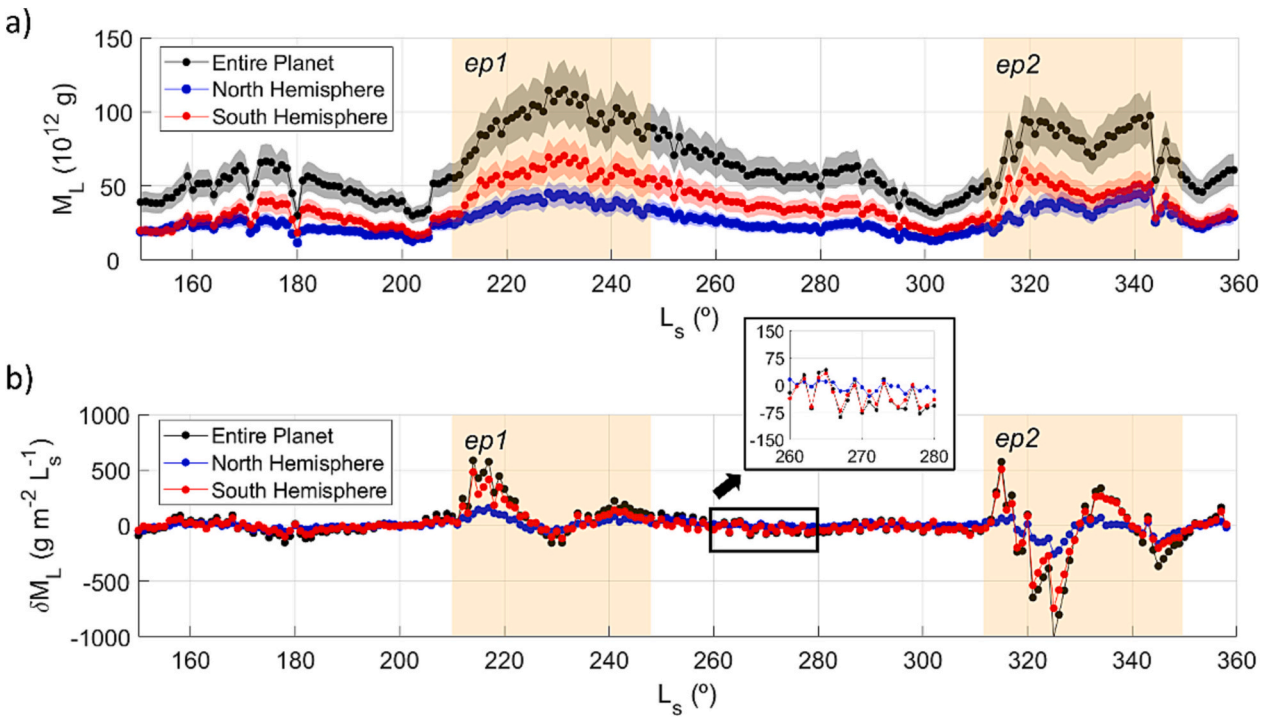

Fig. 1. Planetary scale analysis of the dust cycle during the dusty season: (a) Total mass (M_L; 10^{12} g), and (b) mass lifting-depletion rate (δM_L; g m^{-2} L_s − 1) of dust particles suspended in the atmosphere for each L_s, as integrated for: the entire planet (black dots), the north hemisphere (blue dots) and the south hemisphere (red dots). The shaded coloured bands in (a) represent the uncertainties. Episodes 1 (ep1, from 210° to 245° L_s) and 2 (ep2, from 310° and 350° L_s) are marked by yellow bands. Note that L_s ranges from 150° to 359°, corresponding to the dusty season. The inset shows a close-up view of the short potential dust lifting-depletion rate variability during the period of dust clearing, which shows predominantly a slow, potential negative depletion rate in the southern hemisphere. (For interpretation of the references to colour in this figure legend, the reader is referred to the web version of this article.)

the non-dusty season (particularly, between L_s = 80°-100°; image not shown), being on average 1.8 times greater for the NH. Moreover, the maximum values of M_L are found on the dusty season for both hemispheres (coincident with ep2) and are on average 1.8 times greater for the SH (Fig. 1a). The main sources of dust are located in the SH, and during the dusty season the dust is injected into the atmosphere (Wang and Richardson, 2015). In this climatology, a global-cycle dust storm spreads dust over the planet. As the deposition processes are slow, it is still possible to find values of suspended dust in the NH during the non-dusty season.

Next, we analyse in-depth the ep1 and ep2: from the beginning until the maximum dust loading, M_L increased by almost 60%, reaching approximately 120 10^{12} g (see Fig. 1a). For ep1, the peak was reached progressively, in approximately 40 sols, and the behaviour in both hemispheres was similar, showing a peak value 1.8 times greater in the SH than in the NH. For ep2, a more complex pattern was found, revealing the high variability in this episode that can be attributed to the different occurring time of the C seasonal storm in different MYs; during ~12 sols the total M_L increased, being almost 3 times greater in the SH with respect to NH. After that, M_L progressively decreased during ~26 sols in the SH (but increased in the NH) which could be related to the effective transport of dust from SH to NH. Later on, during ~22 sols, M_L increased in both hemispheres, reaching a peak 1.3 times greater in SH than in NH. Finally, the M_L decreased again, keeping between 20 and 30 10^{12} g at each hemisphere. The mean, maximum and minimum values of M_L for non-dusty and dusty seasons, and ep1 and ep2 are summarized in **Table 2**.

Additionally, Fig. 1b shows the M_L dust lifting-depletion rate (δM_L, g m^{-2} L_s − 1) during the dusty season. As explained in **Sect. 2.4**, the horizontal transport effect cannot be assessed using this methodology. Thus, this work provides an upper bound, and the positive and negative δM_L values are considered potential dust lifting and deposition rates,

Table 2
Mean, maximum and minimum mass loading M_L (in 10^{12} g), integrated over the entire planet and both south (SH) and north hemispheres (NH). M_L was calculated for the entire climatology (i.e., the MY24-MY27 period excluding GDS on MY25; denoted as 'clim'), non-dusty and dusty seasons of the climatology, and during ep1 and ep2. The specific L_s (°) for the max/min M_L values are also shown in brackets.

M_L ($10^{12}g$)	Period	North Hemisphere			South Hemisphere		
		mean	max	min	mean	max	min
Climatology	Whole year (0°-359°)	23 ± 9	47 ± 8	0.006 ± 0.001	28 ± 17	71 ± 36	0.17 ± 0.03
	Non-dusty season (0°-149°)	18 ± 7	34 ± 6	0.006 ± 0.001	13 ± 7	35 ± 7	0.17 ± 0.03
	Dusty season (150°-359°)	27 ± 8	47 ± 8	12 ± 2	38 ± 13	71 ± 36	16 ± 3
Episodes	ep1	37 ± 5	45 ± 8	24 ± 4	57 ± 10	71 ± 36	32 ± 6
	ep2	34 ± 7	47 ± 8	19 ± 3	44 ± 10	60 ± 25	25 ± 4

respectively. If the system is closed, the ratio of the sum of positive and negative δM_L values should be ideally one; that is, at a planetary scale, the same quantity of dust should have been lifted to the atmosphere and deposited on the surface. In this study, this ratio is 0.95 (with more dust deposited than lifted), confirming that this methodology provides an accurate representation of the dust spatio-temporal cycle on Mars. The 5% remaining error can be attributed to the absence of data for different

regions, the resolution limits imposed by the grid (see Sect. 2.1), the error in the retrievals of TES and the rescaling that is done in TES data to 610 Pa to avoid topographic discrepancies, and the large average spatiotemporal approach used in this study (see Sect. 2.3). Taking into account the limiting accuracy of this approach (5% error), all quantitative estimates reported in this work are given only up to two significant values.

This analysis suggests that a total mass of approximately 400 10^{12} g yr^{-1} of dust could be injected into the atmosphere from the entire planet throughout one climatological Martian year. This is calculated by integrating the positive values of δM_L in terms of mass. The dust injection to the atmosphere on Mars is strongly asymmetric, almost 2.5 times greater in the SH than in the NH. It should be noted that this value is presented here as an upper bound, thus dust advection is disregarded in this analysis (see Sect. 2.4).

On Earth, prior global dust models intercomparisons have suggested that dust emissions may range from 500 to 4000 10^{12} g yr^{-1} (Huneeus et al., 2011). However, more recent studies have suggested that the total dust emissions may be as high as 8000 10^{12} g yr^{-1} (Wu et al., 2020a). To summarize, despite the uncertainties in the models and methodologies used, it seems reasonable to conclude that both Mars and Earth can inject comparable amounts of dust into their atmospheres.

These annual dust lifting magnitudes must be put in perspective with the relative differences in area and time used for the calculations. First and foremost, one Martian year is roughly twice as long as an Earth year. Regarding the regions involved in dust lifting, for the case of our analysis on Mars, the region between latitudes 80°S and 80°N was investigated (see Sect. 2.3), which covers a total surface area of approximately 145 million km^2, covered by dry bedrock and regolith. The main dust sources on Earth are deserts, which represent one-third of the 148 million km^2 of the land surface, which suggests that on Earth this amount of dust is produced by a region of about 50 million km^2 (i.e., about 1/3 of the corresponding dust lifting region of Mars).

In both planets, dust is mobilized from the surface into the atmosphere through the exchange of momentum between the surface and the atmosphere. Two mechanisms are believed to predominantly account for the bulk of dust lifting: surface wind stress lifting and dust devils lifting. A detailed information can be found in Newman et al. (2002a) and Gherboudj et al. (2017). The first work models the dust transport processes on Mars, and the second does it on Earth.

3.2. Equivalent dust thickness over the surface

In this section, an estimation of the total thickness of the dust in the Martian atmosphere was performed. We estimate next the height of the dust layer that could be produced if the total amount of dust in suspension, M_L, would be deposited over the surface. Regarding the variability of dust activity over the planet, and according to Forget and Montabone (2017), the locations on Mars with intense dust activity are Hellas region (centred at 43°S 70°E), Argyre Planitia (centred at 50°S 316°E), and both the northern and southern polar regions. The low dust-influenced places were found in a band of ~20° latitude centred around 45°S, the western Meridiani Planum (centred at 0° 358°E) and around the Valles Marineris (centred at 14°S 239°E). It should be noted that the polar regions are not consider in this work, as being out of the scope of valid TES observations (see Sect. 2.1). Thus, as a measure of dust activity, those four specific locations are next examined in depth: Hellas region and Argyre Planitia (as high dust-enhanced zones), and Meridiani Planum and Valles Marineris (as low dust-enhanced zones). For the calculations, an area unity of 2° latitude x 5° longitude centred in their corresponding coordinates is taken. Table 3 shows the coordinates for the four listed locations, together to the mean, maximum and minimum M_L (g m^{-2}) and EDT (μm).

Regarding the dusty season, on average the high dust-enhanced

Table 3
Mean, maximum and minimum mass loading (M_L, g m^{-2}) and equivalent total dust thickness (EDT, μm) values, for two high (Hellas region and Argyre Planitia) and low (Valle Marineris and Meridiani Planum) dust-influenced locations. M_L was calculated for the climatology (i.e., the MY24-MY27) period, non-dusty and dusty seasons, and ep1 and ep2.

			Climatology	non-dusty	dusty	ep1	ep2
					M_L		
High dust-enhanced zones	Hellas Region (43°S, 70°E)	mean	1.3 ± 0.2	1.0 ± 0.2	1.4 ± 0.2	1.9 ± 0.3	1.2 ± 0.2
		max	3.5 ± 0.6	1.7 ± 0.3	3.5 ± 0.6	3.51 ± 0.06	2.6 ± 0.5
		min	0.09 ± 0.02	0.52 ± 0.09	0.09 ± 0.02	1.1 ± 0.2	0.7 ± 0.1
					EDT		
		mean	0.52 ± 0.09	0.40 ± 0.07	0.6 ± 0.1	0.7 ± 0.1	0.48 ± 0.08
		max	1.4 ± 0.3	0.7 ± 0.1	1.4 ± 0.3	1.40 ± 0.02	1.0 ± 0.2
		min	0.04 ± 0.01	0.21 ± 0.04	0.04 ± 0.01	0.42 ± 0.08	0.26 ± 0.04
					M_L		
		mean	1.4 ± 0.3	1.0 ± 0.2	1.5 ± 0.3	1.7 ± 0.3	1.6 ± 0.3
		max	6 ± 1	1.4 ± 0.3	6 ± 1	2.5 ± 0.4	6 ± 1
		min	0.5 ± 0.1	0.7 ± 0.1	0.5 ± 0.1	1.3 ± 0.2	0.5 ± 0.1
	Argyre Planitia (50°S, 316°E)				EDT		
		mean	0.6 ± 0.1	0.42 ± 0.08	0.6 ± 0.1	0.7 ± 0.1	0.6 ± 0.1
		max	2.4 ± 0.4	0.6 ± 0.1	2.4 ± 0.4	1.0 ± 0.2	2.4 ± 0.4
		min	0.22 ± 0.04	0.28 ± 0.05	0.22 ± 0.04	0.53 ± 0.09	0.22 ± 0.04
					M_L		
		mean	0.9 ± 0.2	0.6 ± 0.1	1.2 ± 0.2	1.5 ± 0.3	1.2 ± 0.2
		max	2.6 ± 0.5	1.8 ± 0.3	2.6 ± 0.5	2.6 ± 0.5	2.1 ± 0.4
		min	0.11 ± 0.02	0.11 ± 0.02	0.35 ± 0.06	1.0 ± 0.2	0.7 ± 0.1
	Valle Marineris (0°, 358°E)				EDT		
		mean	0.38 ± 0.07	0.24 ± 0.04	0.47 ± 0.08	0.6 ± 0.1	0.49 ± 0.08
		max	1.0 ± 0.2	0.7 ± 0.1	1.0 ± 0.2	1.0 ± 0.2	0.5 ± 0.2
		min	0.04 ± 0.01	0.04 ± 0.01	0.14 ± 0.02	0.38 ± 0.07	0.29 ± 0.05
Low dust-enhanced zones					M_L		
		mean	1.0 ± 0.2	0.6 ± 0.1	1.2 ± 0.2	1.5 ± 0.3	1.6 ± 0.3
		max	3.5 ± 0.6	1.1 ± 0.2	3.5 ± 0.6	2.6 ± 0.5	3.5 ± 0.6
		min	0.19 ± 0.03	0.19 ± 0.03	0.7 ± 0.1	1.1 ± 0.2	0.8 ± 0.2
	Meridiani Planum (14°S, 239°E)				EDT		
		mean	0.38 ± 0.07	0.22 ± 0.04	0.49 ± 0.09	0.6 ± 0.1	0.6 ± 0.1
		max	1.4 ± 0.3	0.45 ± 0.08	1.4 ± 0.3	1.0 ± 0.2	1.4 ± 0.3
		min	0.08 ± 0.01	0.08 ± 0.01	0.28 ± 0.05	0.42 ± 0.08	0.34 ± 0.06

zones exhibit M_L and EDT values that are 10%–15% higher than those in the low dust-enhanced zones. During this season, the minimum M_L and EDT values are also found in the high dust-enhanced zones.

Focusing on ep1 and ep2 of the dusty season, Hellas region and the low dust-enhanced zones exhibit similar results (mean M_L and EDT values near to 1.5 g m^{-2} and 0.6 μm, respectively). However, those values are 2 times greater at Argyre Planitia, that even reaches maximum M_L and EDT values of almost 6 g m^{-2} and 2.4 μm, respectively. This highlights a higher level of dust activity in Argyre Planitia when compared to the other locations considered in this study.

During the non-dusty season, M_L and EDT values are on average 1.5 times smaller than those found during the dusty-season. This finding applies to both high and low dust-enhanced zones. However, the minimum M_L and EDT values for the latter are found in this season. A possible explanation for this phenomenon may involve the advection of dust into these regions during the dusty season (leading to an observed increase in M_L), which subsequently deposits slowly onto the surface (leading to an observed decrease in M_L).

Fig. 2 shows an estimation of the Equivalent total Dust Thickness (EDT) for ep1 and ep2. During ep1 dust increases throughout the NH and SH in the 70°–130° latitude band, showing values around 0.5 μm (Fig. 2a-first and Fig. 2a-second panels, L_s = 200°-210°). Later, a significant elevation in dust mass is also observed within and immediately south of the equatorial region in the same latitude band (Fig. 2a-third panel, L_s = 210°-215°). Subsequently, this activity not only extends within this latitude band for all longitudes, peaking at L_s = 235°-240° (Fig. 2a-eight panel), with a maximum EDT value of 2.8 μm, but also gives rise to additional hotspots across the planet.

Regarding Hellas Planitia, Valle Marineris and Meridiani Planum their maximum M_L and EDT values occurring during this episode (see Table 3).

During ep2 the greater activity starts in L_s = 320°-325° (Fig. 2b-third panel), with the hot spots mainly concentrated in the SH between longitudes 0°-90° and 270°-359° (orange and red points, EDT ranging from 1.0 μm to 1.5 μm). For L_s = 320°-325° (Fig. 2b-fourth panel) the greater EDT values reaches 30°N at same longitudes, showing maximum EDT values of 10 μm. For the rest of the planet, EDT duplicated their values, reaching 0.6–0.7 μm. Later on, the activity decreases progressively showing values that range from 0.6 to 0.7 μm overall the planet (Fig. 2b-fifth panel, L_s = 325°-335°) to a band ranging from 30°N to 30°S in latitude until the end of the episode (Fig. 2b-eigth panel, L_s = 345°-350°). Note that the maximum M_L and EDT values occurring during this episode at Argyre Planitia, were estimated to be 6 g m^{-2} and 1.4 μm, respectively (see Table 3).

The accumulated dust layer deposited on the surface, over the bedrock or regolith, plays a crucial role on Mars. The dust forms an interface between the ground and the atmosphere, likely interacting with atmospheric moisture and other volatiles, masking the photometric signatures of underlying rocks, and affecting the emissivity and albedo of the region. Also, this dust layer can participate in new dust lifting processes and be transported elsewhere. With the aim of estimating the EDT deposited in the four Martian regions under study, an area unity of 2° latitude x 5° longitude has been selected, centred in their corresponding coordinates (see Table 3). Over this area, the negative δM_L

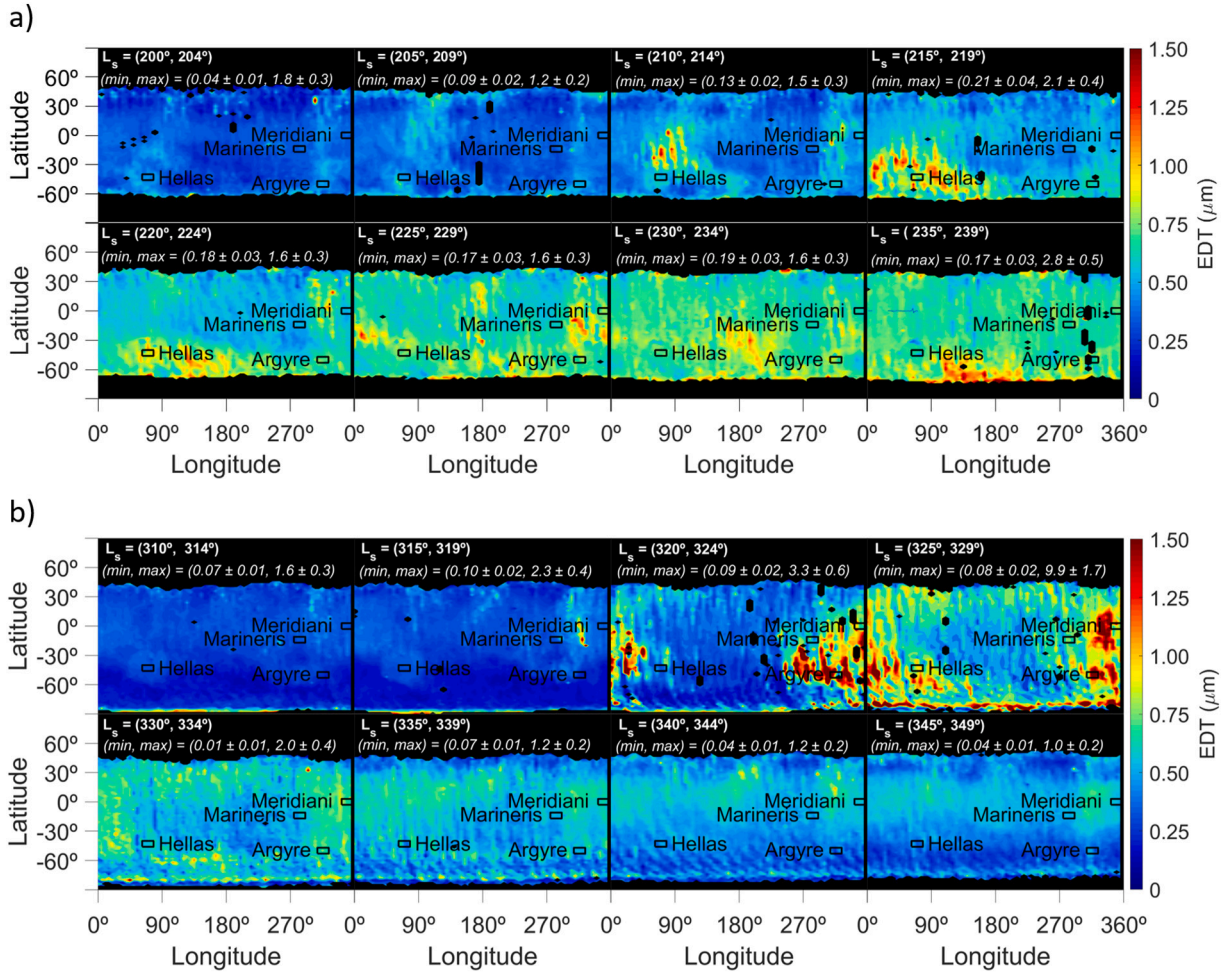

Fig. 2. Equivalent total dust thickness (EDT) (in μm) of atmospheric dust in suspension: (a) ep1 as shown averaging 5° L_s for L_s range 200°-240°, and (b) ep2 as shown averaging 5° L_s for L_s range 310°-350°. The maximum and minimum EDT values are also included.

values have been integrated during the climatology. It is worth noting that this calculation provides an upper bound for EDT, as no dynamic transport has been considered (see **Sect. 2.3**). Thus, an estimation of EDT of about 80–100 μm for the low dust-enhanced zones, and of 50-60 μm for the high dust-enhance zones, has been found.

Those results can be compared to in-situ observations. Taking into consideration the MER rovers, which were located into Gusev Crater and Meridiani Planum (both low dust-enhanced zones), Madsen et al. (2009) reported that the accumulated dust deposition over the magnetic parts of the rovers reached a layer <50 μm thick (clean alumina) and 50–100 μm thick (magnets), accumulated over a period of several hundreds of sols.

3.3. Dust lifting-depletion rate: case studies

To determine the regional distribution of dust sources on Mars, Fig. 3 illustrates a mapping of the dust lifting-depletion rate of ep1 and ep2 (Figs. 3a-3b). For a clear representation, M_L values were previously calculated accumulating the data over periods of 5° L_s (see **Sect. 2.3**). The rate δM_L is calculated by subtracting and dividing over the intermediate period of time and is given in g m^{-2} $L_s - 1$. The transition from warmer (reddish) to cooler (blueish) colours corresponds to a change of those δM_L differences. Positive (negative) δM_L values may represent a dust source (sink), or an incoming transport through the atmosphere.

Regarding ep1 (Fig. 3a), at the beginning of the episode (Fig. 3a-second panel, L_s = 205°-215°) the areas with more activity were found mainly in SH in a band of 12°N-50°S latitude and (50°-125°, 300°-330°) longitude. A few sols later the activity increased in a band of 0°-180° in the SH, showing an δM_L that ranges from positive to negative values of 0.2–0.5 g m^{-2} $L_s - 1$ (Fig. 3a-third panel and Fig. 3a-fourth panel). During the rest of the episode, several spots with dust activity can be found in both NH and SH.

During ep2 the great dust activity was found in a band of 0º-80º and 240º-360º longitude, mostly in SH (Fig. 3b-second and third panels, L_s = 315°-330°). The δM_L values reaches in some areas maximum values of 1.5 g m^{-2} L_s^{-1} (**Fig. 3**b-second panel), peaking even 4.8 g m^{-2} L_s^{-1} (Fig. 3b-third panel). The minimum (negative) values are found for L_s = 325°-335° (Fig. 3b-fourth panel). During the rest of the episode, δM_L ranges between ±0.15 g m^{-2} L_s^{-1}.

Looking at Fig. 3, some regions might stand out persistently as dust sinks or sources, or pathways of dust transport. However, this methodology does not permit to distinguish between them (see **Sect. 2.4**). Starting from a neutral situation ($\delta M_L = 0$) at a certain location, an increase in the M_L values could be related to a dust lifting (source) or transport of the dust over the location, originated in another source point. Moreover, a decrease in the M_L values could be related to the

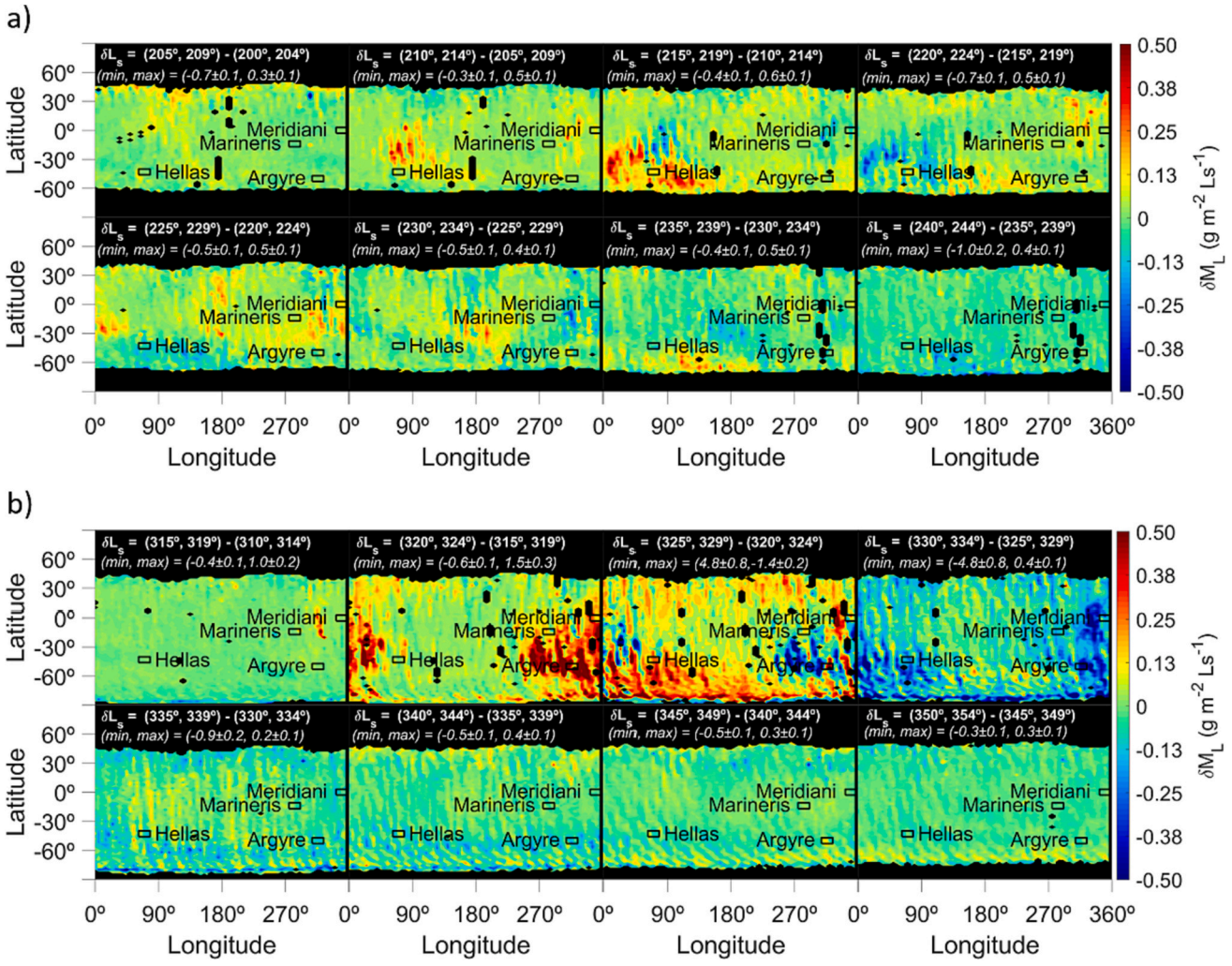

Fig. 3. Potential dust lifting (or depletion) rates, together with transport, for two different seasonal periods as represented by the difference between consecutive M_L (g m^{-2}) values (δM_L, g m^{-2} L_s^{-1}): (a) ep1 as shown averaging 5° L_s for L_s range 200°-240°, and (b) ep2 as shown averaging 5° L_s for L_s range 310°-350°. Positive/negative δM_L values represent possible dust lifting/depletion Martian zones (from red to blue colours). The maximum and minimum δM_L values are also included. (For interpretation of the references to colour in this figure legend, the reader is referred to the web version of this article.)

deposition of the dust (sink) or, as before, to the transport of dust to another location. In order to differentiate them, the potential sinks and sources present in this work are compared with other studies.

One interesting period for finding dust-lifting sources with this methodology could be ep1, as at the beginning of this time the atmosphere is clear. Fig. 4 shows the proposed sources found with our methodology together with 100 top dust source grid points, responsible for contributing the greatest dust mass to the atmosphere in FINDUST. Particularly, they represent the MY 21–30 period of the FINDUST Stage O model (Newman and Richardson, 2015) (white crosses in Fig. 4). In this study, a point was considered a potential source if it fulfilled that $\delta M_L > 0.15$ g m^{-2} L$_s$ − 1 during ep1. The source spots were mainly located for (20°S-60°S) latitudes and (0°-160°) longitudes; 70% of FINDUST modelled sources agree with those in this study. Our analysis finds other locations of intense dust-lifting activity which are not captured in the FINDUST models and could be related to the dust advection that cannot be distinguish by the methodology used in this work. Our analysis can be used to fine-tune some of the free parameters for global circulation models with interactive dust cycles, performing sensitivity analysis that can confirm a similar distribution of dust sources and sinks. See, for instance, Gebhardt et al. (2020) for a sensitivity analysis of dust-interactive models where the dust devil lifting, the wind stress lifting threshold and the wind stress lifting rate constant have to be tuned to produce a reasonable climatology. These interactive dust lifting parameters sensitively depend on the model resolution and must be determined individually for any model configuration by a trial-and-error approach.

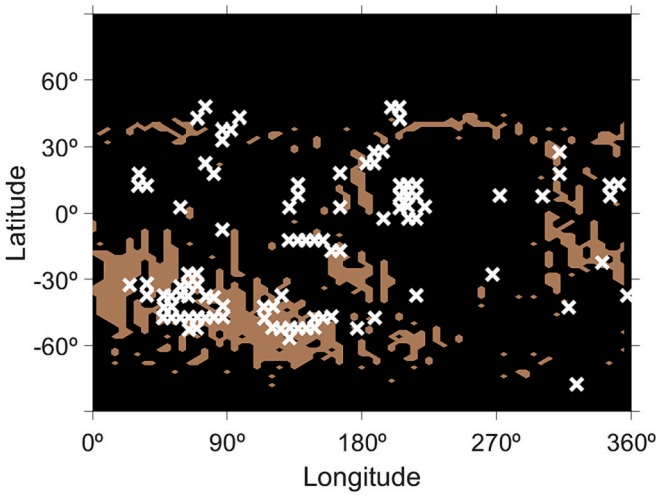

Fig. 4. *Potential dust sources with $\delta M_L > 0.15$ g m^{-2} L$_s^{-1}$ (light brown) for ep1 together with the top 100 dust sources grid points for MY 21–30 of FINDUST Stage O model (white crosses) as reported in* Newman and Richardson (2015). (For interpretation of the references to colour in this figure legend, the reader is referred to the web version of this article.)

4. Summary and conclusions

This study has put forward a methodology to estimate the total atmospheric dust mass loading using remote sensing opacity measurements. As an example, the opacity database provided by the Thermal Emission Spectrometer (TES) was used. However, this study can be applied to other dust databases as well, including the orbital missions that are currently observing the atmosphere of the planet. Thus, future work would address it, for example with the database created by Montabone et al. (2015) by using measurements from different instruments. The results produced by this procedure have been cross-validated by comparing with Earth atmospheric studies and with in-situ measurements of the dust accumulation over surfaces, providing reasonable comparisons. The dust mass conversion factors are well-characterized on Earth. Using this knowledge, we proposed a mass conversion factor of 1.9 ± 0.3 g m^{-2} (per unit of dust opacity) in this study. The methodology is not capable of disentangling completely the effects of dust lifting/depletion and dust advection. Thus, all results provides an upper bound of the properties under study.

As a result of the atmospheric circulation processes, the southern hemisphere contained up to three times more atmospheric dust mass than the northern hemisphere. This annually lifted, long-range transported and sedimented amount of dust must be a source of continuous redistribution of mass over the whole planet, transporting dust particles from the southern to the northern hemisphere. An estimation of about 400 10^{12} g of dust can circulate throughout the Martian atmosphere every year. This amount is comparable to the equivalent estimated amounts of atmospheric dust on Earth, which can vary between 500 and 8000 10^{12} g yr^{-1} depending on the studies.

The procedure that is here described, and has been validated, can be used to map dust sources and fine-tune, by comparison, the dust-lifting efficiency factors as well as the threshold wind stress parameters of global circulation models with interactive dust cycles, such as FINDUST. The analysis of the changes in TES dust opacity showed several atmospheric dust sources that are 70% coincided with the simulations of the FINDUST model for identifying dust sources.

By considering the potential deposited dust on the low dust-enhanced zones used as an example in this study (Valle Marineris and Meridiani Planum), the dust seemed to deposit progressively during the climatological year, with an estimation of the equivalent total dust layer thickness of 100 μm. This magnitude is comparable with the estimates of the accumulated dust deposition over the magnetic parts of the MER rovers, which reported the formation of layers <50 μm thick over clean alumina and 50–100 μm thick over magnets. The results of accumulated dust deposition can be relevant in relation to Mars' habitability because a dust layer of a few micrometers (μm) is enough to shield from UV radiation, and thus all materials, including potential microorganisms, will eventually be shielded underneath the annually accumulated layer of dust.

The mobilized fraction of dust is homogenised globally although there are a few dominant dust sources on the planet. Our analysis is consistent with the homogeneous dust composition observed by different in-situ missions operating on the surface of Mars at different sites, which suggests that the sustained atmospheric redistribution of dust has resulted in a planet-wide homogenization of the dust cover.

Finally, this multiannual circulation of dust, interacting with the UV radiation and atmospheric chemistry, and being transported over long distances and accumulating on the ground surface (in amounts of approximately 100–200 g m^{-2}), must be relevant for the present-day surface chemistry, mineral distribution and for planetary protection policies, as any putative terrestrial contamination brought with spacecraft may be transported over long distance shielded from the incident UV radiation by the dust.

Declaration of Competing Interest

The authors declare that they have no known competing financial interests or personal relationships that could have appeared to influence the work reported in this paper.

Data availability

The TES database is available in the Mars Global Data Sets (http://tes.asu.edu/data_tool/).

Acknowledgements

This work is supported by grant PID2019-104205GB-C21 funded by MCIN/AEI/10.13039/501100011033 (CAMELIA project). M.-P. Z. was

supported by grant PID2022-140180OB-C21 funded by MCIN /AEI /10.13039/501100011033 / FEDER, UE. MÁLC is supported by the INTA predoctoral contract program. Authors are really grateful for the two anonymous referees' comments that definitively improved the study.

References

Albani, S., Mahowald, N.M., 2019. Paleodust insights into dust impacts on climate. J. Clim. 32, 7897–7913. https://doi.org/10.1175/JCLI-D-18-0742.1.

Ansmann, A., Mamouri, R.-E., Hofer, J., Baars, H., Althausen, D., Abdullaev, S.F., 2019. Dust mass, cloud condensation nuclei, and ice-nucleating particle profiling with polarization lidar: updated POLIPHON conversion factors from global AERONET analysis. Atmos. Meas. Tech. 12, 4849–4865. https://doi.org/10.5194/amt-12-4849-2019.

Atreya, S.K., Wong, A.-S., Renno, N.O., Farrell, W.M., Delory, G.T., Sentman, D.D., Cummer, S.A., Marshall, J.R., Rafkin, S.C.R., Catling, D.C., 2006. Oxidant enhancement in Martian dust devils and storms: implications for life and habitability. Astrobiology 6, 439–450. https://doi.org/10.1089/ast.2006.6.439.

Battalio, M., Wang, H., 2021. The Mars Dust Activity Database (MDAD): a comprehensive statistical study of dust storm sequences. Icarus 354, 114059. https://doi.org/10.1016/j.icarus.2020.114059.

Bertrand, T., Wilson, R.J., Kahre, M.A., Urata, R., Kling, A., 2020. Simulation of the 2018 global dust storm on Mars using the NASA Ames Mars GCM: a multitracer approach. J. Geophys. Res. Planets 125 (7). https://doi.org/10.1029/2019JE006122.

Birney, D.S., Gonzalez, G., Oesper, D., 2006. Observational Astronomy. Cambridge University Press.

Chassefiére, E., Leblanc, F., 2004. Mars atmospheric escape and evolution; interaction with the solar wind. Planet. Space Sci. 52 (11), 1039–1058. https://doi.org/10.1016/j.pss.2004.07.002.

Chen-Chen, H., Pérez-Hoyos, S., Sánchez-Lavega, A., 2021. Dust particle size, shape and optical depth during the 2018/MY34 martian global dust storm retrieved by MSL Curiosity rover Navigation Cameras. Icarus 354, 114021. https://doi.org/10.1016/j.icarus.2020.114021.

Christensen, P.R., 1986. The spatial distribution of rocks on mars. Icarus 68, 217–238. https://doi.org/10.1016/0019-1035(86)90020-5.

Christensen, P.R., Bandfield, J.L., Hamilton, V.E., Ruff, S.W., Kieffer, H.H., Titus, T.N., Malin, M.C., Morris, R.V., Lane, M.D., Clark, R.L., Jakosky, B.M., Mellon, M.T., Pearl, J.C., Conrath, B.J., Smith, M.D., Clancy, R.T., Kuzmin, R.O., Roush, T., Mehall, G.L., Gorelick, N., Bender, K., Murray, K., Dason, S., Greene, E., Silverman, S., Greenfield, M., 2001. Mars global surveyor thermal emission spectrometer experiment: investigation description and surface science results. J. Geophys. Res. Planets 106, 23823–23871. https://doi.org/10.1029/2000JE001370.

Clancy, R.T., Wolff, M.J., Christensen, P.R., 2003. Mars aerosol studies with the MGS TES emission phase function observations: optical depths, particle sizes, and ice cloud types versus latitude and solar longitude. J. Geophys. Res. Planets 108. https://doi.org/10.1029/2003JE002058.

Clancy, R.T., Wolff, M.J., Whitney, B.A., Cantor, B.A., Smith, M.D., McConnochie, T.H., 2010. Extension of atmospheric dust loading to high altitudes during the 2001 Mars dust storm: MGS TES limb observations. Icarus 207 (11), 98–109. https://doi.org/10.1016/j.icarus.2009.10.011.

Córdoba-Jabonero, C., Lara, L.M., Mancho, A.M., Márquez, A., Rodrigo, R., 2003. Solar ultraviolet transfer in the Martian atmosphere: biological and geological implications. Planet. Space Sci. 51, 399–410. https://doi.org/10.1016/S0032-0633(03)00023-0.

Córdoba-Jabonero, C., Zorzano, M.-P., Selsis, F., Patel, M.R., Cockell, C.S., 2005. Radiative habitable zones in martian polar environments. Icarus 175, 360–371. https://doi.org/10.1016/j.icarus.2004.12.009.

DeMott, P.J., Sassen, K., Poellot, M.R., Baumgardner, D., Rogers, D.C., Brooks, S.D., Prenni, A.J., Kreidenweis, S.M., 2003. African dust aerosols as atmospheric ice nuclei. Geophys. Res. Lett. 30 https://doi.org/10.1029/2003GL017410.

Dubovik, O., King, M.D., 2000. A flexible inversion algorithm for retrieval of aerosol optical properties from sun and sky radiance measurements. J. Geophys. Res.-Atmos. 105, 20673–20696. https://doi.org/10.1029/2000JD900282.

Fenton, L.K., Geissler, P.E., Haberle, R.M., 2007. Global warming and climate forcing by recent albedo changes on Mars. Nature 446, 646–649. https://doi.org/10.1038/nature05718.

Fenton, L., Reiss, D., Lemmon, M., Marticorena, B., Lewis, S., Cantor, B., 2016. Orbital observations of dust lofted by daytime convective turbulence. Space Sci. Rev. 203, 89–142. https://doi.org/10.1007/s11214-016-0243-6.

Forget, F., Montabone, L., 2017. Atmospheric Dust on Mars: A Review.47th International Conference on Environmental Systems.

Gebhardt, C., Abuelgasim, A., Fonseca, R.M., Martín-Torres, J., Zorzano, M.-P., 2020. Fully interactive and refined resolution simulations of the Martian dust cycle by the MarsWRF model. J. Geophys. Res. Planets 125 (9). https://doi.org/10.1019/2019JE006253.

Gherboudj, I., Beegum, S.N., Ghedira, H., 2017. Identifying natural dust source regions over the Middle-East and North Africa: estimations of dust emission potential. Earth-science Rev. 165, 342–355. https://doi.org/10.1016/j.earscirev.2016.12.010.

Giles, D.M., Sinyuk, A., Sorokin, M.G., Schafer, J.S., Smirnov, A., Slutsker, I., Eck, T.F., Holben, B.N., Lewis, J.R., Campbell, J.R., Welton, E.J., Korkin, S.V., Lyapustin, A.I., 2019. Advancements in the Aerosol Robotic Network (AERONET) Version 3 database – automated near-real-time quality control algorithm with improved cloud screening for Sun photometer aerosol optical depth (AOD) measurements. Atmos. Meas. Tech. 12, 169–209. https://doi.org/10.5194/amt-12-169-2019.

Guzewich, S.D., Toigo, A.D., Richardson, M.I., Newman, C.E., Talaat, E.R., Waugh, D.W., McConnochie, T.H., 2013. The impact of a realistic vertical dust distribution on the simulation of the Martian General Circulation. J. Geophys. Res. Planets 118, 980–993. https://doi.org/10.1002/jgre.20084.

Haberle, R.M., 1986. Interannual variability of global dust storms on Mars. Science 234, 459–461. https://doi.org/10.1126/science.234.4775.459.

Haberle, R.M., Kahre, M.A., Hollingsworth, J.L., Montmessin, F., Wilson, R.J., Urata, R. A., Brecht, A.S., Wolff, M.J., Kling, A.M., Schaeffer, J.R., 2019. Documentation of the NASA/Ames Legacy Mars Global Climate Model: simulations of the present seasonal water cycle. Icarus 333, 130–164. https://doi.org/10.1016/j.icarus.2019.03.026.

Hart, M.H., 1978. The evolution of the atmosphere of the earth. Icarus. 33 (1), 23–39. https://doi.org/10.1016/0019-1035(78)90021-0.

Heavens, N.G., Richardson, M.I., Kleinböhl, A., Kass, D.M., McCleese, D.J., Abdou, W., Benson, J.L., Schofield, J.T., Shirley, J.H., Wolkenberg, P.M., 2011. The vertical distribution of dust in the Martian atmosphere during northern spring and summer: observations by the Mars climate sounder and analysis of zonal average vertical dust profiles. J. Geophys. Res. 116, E04003. https://doi.org/10.1029/2010JE003691.

Hess, M., Koepke, P., Schult, I., 1998. Optical properties of aerosols and clouds: the software package OPAC. Bull. Am. Meteorol. Soc. 79, 831–844.

Holben, B.N., Eck, T.F., al Slutsker, I., Tanre, D., Buis, J.P., Setzer, A., Vermote, E., Reagan, J.A., Kaufman, Y.J., Nakajima, T., 1998. AERONET—A federated instrument network and data archive for aerosol characterization. Remote Sens. Environ. 66, 1–16. https://doi.org/10.1016/S0034-4257(98)00031-5.

Holmes, J.A., Lewis, S.R., Patel, M.R., Chaffin, M.S., Cangi, E.M., Deighan, J., Schneider, N.M., Aoki, S., Fedorova, A.A., Kass, D.M., Vandaele, A.C., 2021. Enhanced water loss from the martian atmosphere during a regional-scale dust storm and implications for long-term water loss. Earth Planet. Sci. Lett. 571, 117109 https://doi.org/10.1016/j.epsl.2021.117109.

Huneeus, N., Schulz, M., Balkanski, Y., Griesfeller, J., Prospero, J., Kinne, S., Bauer, S., Boucher, O., Chin, M., Dentener, F., Diehl, T., Easter, R., Fillmore, D., Ghan, S., Ginoux, P., Grini, A., Horowitz, L., Koch, D., Krol, M.C., Landing, W., Liu, X., Mahowald, N., Miller, R., Morcrette, J.-J., Myhre, G., Penner, J., Perlwitz, J., Stier, P., Takemura, T., Zender, C.S., 2011. Global dust model intercomparison in AeroCom phase I. Atmos. Chem. Phys. 11, 7781–7816. https://doi.org/10.5194/acp-11-7781-2011.

Husar, R.B., Prospero, J.M., Stowe, L.L., 1997. Characterization of tropospheric aerosols over the oceans with the NOAA advanced very high resolution radiometer optical thickness operational product. J. Geophys. Res.-Atmos. 102, 16889–16909. https://doi.org/10.1029/96JD04009.

Jakosky, B.M., Mellon, M.T., Kieffer, H.H., Christensen, P.R., Varnes, E.S., Lee, S.W., 2000. The thermal inertia of Mars from the Mars global surveyor thermal emission spectrometer. J. Geophys. Res. Planets 105, 9643–9652. https://doi.org/10.1029/1999JE001088.

Jankowiak, I., Tanré, D., 1992. Satellite climatology of Saharan dust outbreaks: method and preliminary results. J. Clim. 5, 646–656. https://doi.org/10.1175/1520-0442(1992)005<0646:SCOSDO>2.0.CO;2.

Jeong, G.Y., Kim, J.Y., Seo, J., Kim, G.M., Jin, H.C., Chun, Y., 2014. Long-range transport of giant particles in Asian dust identified by physical, mineralogical, and meteorological analysis. Atmos. Chem. Phys. 14, 505–521. https://doi.org/10.5194/acp-14-505-2014.

Kahre, M.A., Murphy, J.R., Haberle, R.M., 2006. Modeling the Martian dust cycle and surface dust reservoirs with the NASA Ames general circulation model. J. Geophys. Res. Planets 111. https://doi.org/10.1029/2005JE002588.

Kahre, M.A., Murphy, J.R., Newman, C.E., Wilson, R.J., Cantor, B.A., Lemmon, M.T., Wolff, M.J., 2017. The Mars dust cycle. In: Forget, F., Smith, M.D., Clancy, R.T., Zurek, R.W., Haberle, R.M. (Eds.), The Atmosphere and Climate of Mars. Cambridge Planetary Science. Cambridge University Press, Cambridge, pp. 295–337. https://doi.org/10.1017/9781139060172.010.

Karydis, V.A., Kumar, P., Barahona, D., Sokolik, I.N., Nenes, A., 2013. Assessing the impact of mineral dust and adsorption activation on cloud droplet formation. In: Helmis, C.G., Nastos, P.T. (Eds.), Advances in Meteorology, Climatology and Atmospheric Physics, Springer Atmospheric Sciences. Springer, Berlin, Heidelberg, pp. 515–520. https://doi.org/10.1007/978-3-642-29172-2_73.

Kass, D., Kleinböhl, A., McCleese, D., Schofield, J., Smith, M., 2016. Interannual similarity in the Martian atmosphere during the dust storm season. Geophys. Res. Lett. 43 (12), 6111–6118. https://doi.org/10.1002/2016GL068978.

Kleinböhl, A., Abdou, W.A., Schofield, J.T., Kass, D.M., McCleese, D.J., 2009. Mars Climate Sounder limb retrievals of dust and water ice using scattering radiative transfer: Implications for particle size. Cent, Mountain View, Calif, pp. 15–17.

Kleinböhl, A., Spiga, A., Kass, D.M., Shirley, J.H., Millou, E., Montbone, L., Forget, F., 2020. Diurnal variations of dust during the 2018 global dust storm observed by the Mars Climate Sounder. J. Geophys. Res. Planets 125 (1). https://doi.org/10.1029/2019JE006115.

Krasnopolsky, V.A., 2011. Atmospheric chemistry on Venus, Earth, and Mars: Main features and comparison. Planet. Space Sci., Comparative Planetology: Venus-Earth-Mars 59, 952–964. https://doi.org/10.1016/j.pss.2010.02.011.

Lemmon, M.T., Wolff, M.J., Smith, M.D., Clancy, R.T., Banfield, D., Landis, G.A., Ghosh, A., Smith, P.H., Spanovich, N., Whitney, B., Whelley, P., Greeley, R., Thompson, S., Bell, J.F., Squyres, S.W., 2004. Atmospheric imaging results from the Mars exploration rovers: spirit and opportunity. Science 306, 1753–1756. https://doi.org/10.1126/science.1104474.

Lemmon, M.T., Wolff, M.J., Bell, J.F., Smith, M.D., Cantor, B.A., Smith, P.H., 2015. Dust aerosol, clouds, and the atmospheric optical depth record over 5 Mars years of the

Mars Exploration Rover mission. Icarus, Dynamic Mars 251, 96–111. https://doi.org/10.1016/j.icarus.2014.03.029.
Leovy, C., 2001. Weather and climate on Mars. Nature 412, 245–249. https://doi.org/10.1038/35084192.
Madsen, M.B., Goetz, W., Bertelsen, P., Binau, C.S., Folkmann, F., Gunnlaugsson, H.P., Í Hjøllum, J., Hviid, S.F., Jensen, J., Kinch, K.M., Leer, K., Madsen, D.E., Merrison, J., Olsen, M., Arneson, H.M., Bell III, J.F., Gellert, R., Herkenhoff, K.E., Johnson, J.R., Johnson, M.J., Klingelhöfer, G., McCartney, E., Ming, D.W., Morris, R.V., Proton, J. B., Rodionov, D., Sims, M., Squyres, S.W., Wdowiak, T., Yen, A.S., 2009. Overview of the magnetic properties experiments on the Mars Exploration Rovers. J. Geophys. Res. Planets 114. https://doi.org/10.1029/2008JE003098.
Mamouri, R.-E., Ansmann, A., 2014. Fine and coarse dust separation with polarization lidar. Atmos. Meas. Tech 7, 3717–3735. https://doi.org/10.5194/amt-7-3717-2014.
Mamouri, R.-E., Ansmann, A., 2017. Potential of polarization/Raman lidar to separate fine dust, coarse dust, maritime, and anthropogenic aerosol profiles. Atmos. Meas. Tech. 10, 3403–3427. https://doi.org/10.5194/amt-10-3403-2017.
Mangold, N., Ansan, V., Masson, P., Vincendon, C., 2009. Estimate of aeolian dust thickness in Arabia Terra, Mars: implications of a thick mantle (> 20 m) for hydrogen detection. Géomorphologie Relief Process. Environ. 15, 23–32. https://doi.org/10.4000/geomorphologie.7472.
Montabone, L., Forget, F., Millour, E., Wilson, R.J., Lewis, S.R., Cantor, B., Kass, D., Kleinböhl, A., Lemmon, M.T., Smith, M.D., Wolff, M.J., 2015. Eight-year climatology of dust optical depth on Mars. Icarus, Dynamic Mars 251, 65–95. https://doi.org/10.1016/j.icarus.2014.12.034.
Montabone, L., Spiga, A., Kass, D.M., Kleinböhl, A., Forget, F., Millour, E., 2020. Martian year 34 column dust climatology from Mars climate sounder observations: reconstructed maps and models simulations. J. Geophys. Res. Planets 125 (8). https://doi.org/10.1029/2019JE006111.
Newman, C.E., Richardson, M.I., 2015. The impact of surface dust source exhaustion on the martian dust cycle, dust storms and interannual variability, as simulated by the MarsWRF General Circulation Model. Icarus 257, 47–87. https://doi.org/10.1016/j.icarus.2015.03.030.
Newman, C.E., Lewis, S.R., Read, P.L., Forget, F., 2002a. Modeling the Martian dust cycle 1. Representation of dust transport processes. J. Geophys. Res. Planets 107 (E12). https://doi.org/10.1029/2002JE001910, 6–1.
Newman, C.E., Lewis, S.R., Read, P.L., Forget, F., 2002b. Modeling the Martian dust cycle 2. Multiannual radiatively active dust transport simulations. J. Geophys. Res. Planets 107. https://doi.org/10.1029/2002JE001920, 7-1-7–15.
Olsson-Francis, K., Doran, P.T., Ilyin, V., Raulin, F., Rettberg, P., Kminek, G., Mier, M.-P. Z., Coustenis, A., Hedman, N., Shehhi, O.A., Ammannito, E., Bernardini, J., Fujimoto, M., Grasset, O., Groen, F., Hayes, A., Gallagher, S., Kumar, K.P., Mustin, C., Nakamura, A., Seasly, E., Suzuki, Y., Peng, J., Prieto-Ballesteros, O., Sinibaldi, S., Xu, K., Zaitsev, M., 2023. The COSPAR planetary protection policy for robotic missions to Mars: a review of current scientific knowledge and future perspectives. Life Sci. Space Res. 36, 27–35. https://doi.org/10.1016/j.lssr.2022.12.001.
Read, P.L., Lewis, S.R., 2004. The Martian Climate Revisited: Atmosphere and Environment of a Desert Planet. Springer Science & Business Media.
Schuster, G.L., Vaughan, M., MacDonnell, D., Su, W., Winker, D., Dubovik, O., Lapyonok, T., Trepte, C., 2012. Comparison of CALIPSO aerosol optical depth retrievals to AERONET measurements, and a climatology for the lidar ratio of dust. Atmos. Chem. Phys. 12, 7431–7452. https://doi.org/10.5194/acp-12-7431-2012.
Sheel, V., Haider, S.A., 2016. Long-term variability of dust optical depths on Mars during MY24–MY32 and their impact on subtropical lower ionosphere: climatology, modeling, and observations. J. Geophys. Res. Space Physics 121, 8038–8054. https://doi.org/10.1002/2015JA022300.
Shirley, J.H., Newman, C.E., Mischna, M.A., Richardson, M.I., 2019. Replication of the historic record of martian global dust storm occurrence in an atmospheric general circulation model. Icarus 317, 197–208. https://doi.org/10.1016/j.icarus.2018.07.024.
Sinyuk, A., Holben, B.N., Eck, T.F., Giles, D.M., Slutsker, I., Korkin, S., Schafer, J.S., Smirnov, A., Sorokin, M., Lyapustin, A., 2020. The AERONET version 3 aerosol retrieval algorithm, associated uncertainties and comparisons to version 2. Atmos. Meas. Tech. 13, 3375–3411. https://doi.org/10.5194/amt-13-3375-2020.
Smith, M.D., 2004. Interannual variability in TES atmospheric observations of Mars during 1999–2003. Icarus 167, 148–165. https://doi.org/10.1016/j.icarus.2003.09.010.
Smith, M.D., Pearl, J.C., Conrath, B.J., Christensen, P.R., 2000. Mars Global Surveyor Thermal Emission Spectrometer (TES) observations of dust opacity during aerobraking and science phasing. J. Geophys. Res. Planets 105, 9539–9552. https://doi.org/10.1029/1999JE001097.
Stevens, B., 2015. Rethinking the lower bound on aerosol radiative forcing. J. Clim. 18, 4794–4819. https://doi.org/10.1175/JCLI-D-14-00656.1.
Swap, R., Garstang, M., Greco, S., Talbot, R., Kållberg, P., 1992. Saharan dust in the Amazon Basin. Tellus B 44, 133–149. https://doi.org/10.1034/j.1600-0889.1992.t01-1-00005.x.
Wang, H., Richardson, M.I., 2015. The origin, evolution, and trajectory of large dust storms on Mars during Mars years 24–30 (1999–2011). Icarus, Dynamic Mars 251, 112–127. https://doi.org/10.1016/j.icarus.2013.10.033.
Wang, Y., Chow, K.-C., Xiao, J., Wong, C.-F., 2021. Effect of dust particle size on the climate of Mars. Planet. Space Sci. 208, 105346 https://doi.org/10.1016/j.pss.2021.105346.
Wolff, M.J., Clancy, R.T., 2003. Constraints on the size of Martian aerosols from Thermal Emission Spectrometer observations. J. Geophys. Res. Planets 108. https://doi.org/10.1029/2003JE002057.
Wolff, M.J., Smith, M.D., Clancy, R.T., Spanovich, N., Whitney, B.A., Lemmon, M.T., Bandfield, J.L., Banfield, D., Ghosh, A., Landis, G., Christensen, P.R., Bell III, J.F., Squyres, S.W., 2006. Constraints on dust aerosols from the Mars Exploration Rovers using MGS overflights and Mini-TES. J. Geophys. Res. Planets 111. https://doi.org/10.1029/2006JE002786.
Wolff, M.J., Smith, M.D., Clancy, R.T., Arvidson, R., Kahre, M., Seelos IV, F., Murchie, S., Savijärvi, H., 2009. Wavelength dependence of dust aerosol single scattering albedo as observed by the Compact Reconnaissance Imaging Spectrometer. J. Geophys. Res. Planets 114. https://doi.org/10.1029/2009JE003350.
Wu, C., Lin, Z., Liu, X., 2020a. The global dust cycle and uncertainty in CMIP5 (coupled model Intercomparison project phase 5) models. Atmos. Chem. Phys. 20, 10401–10425. https://doi.org/10.5194/acp-20-10401-2020.
Wu, Z., Li, T., Zhang, X., Li, J., Cui, J., 2020b. Dust tides and rapid meridional motions in the Martian atmosphere during major dust storms. Nature Comm. 11 (1), 614. https://doi.org/10.1038/s41467-020-14510-x.
Zorzano, M.-P., Córdoba-Jabonero, C., 2007. Influence of aerosol multiple scattering of ultraviolet radiation on martian atmospheric sensing. Icarus, Deep Impact Mission to Comet 9P/Tempel 1, Part 2 190, 492–503. https://doi.org/10.1016/j.icarus.2007.03.029.